First-principles calculations on CuInSe 2 /AlP heterostructures

Pingping Jiang, Marie-Christine Record, P. Boulet

First-principle calculations on $CuInSe_2$/AlP heterostructures

Pingping JIANG [a,b], *Marie-Christine RECORD* [b*], *Pascal BOULET* [a]

[a] Aix-Marseille University, CNRS, MADIREL, Marseille, France

[b] Aix-Marseille University, University of Toulon, CNRS, IM2NP, Marseille, France

Abstract: Heterostructures based on $CuInSe_2$ absorber with AlP buffer have been modeled for the first time by different stacking schemes and interfacial terminations. Mechanical, electronic and topological properties of $CuInSe_2$/AlP heterostructures along [001] direction were investigated using full potential linear augmented plane wave (FP-LAPW) method. Optimal interfacial distance, thermodynamic stability and band alignment have been computed systematically. Heterointerface at "on-top" stacking is the most thermodynamically stable compared with other stackings. The magnitudes of core level binding energy differences are in accordance with interfacial adhesion energies. Absolute deformation potentials ADPs of band energies as a function of (001) biaxial strain were determined. With redressing ADPs, the revised valence and conduction band offsets have increased and decreased, respectively. AlP has strong resistance to biaxial strain in the evolution of band energy edges. Topological properties and density of states were used to investigate the relationship between interatomic interactions and energy band evolution. The most stable $CuInSe_2$/AlP heterostructures have "spike-like" band offsets, with the one terminated as Se-Al characterized by a flat conduction band offset of 12 meV. This comes from the strong "Cu d-Se p" states hybridization. The theoretical maximum conversion efficiency of AlP-based "absorber-buffer" heterostructure is 27. 39% at 0.5 μm thickness.

Keywords: Buffer layer; heterostructure; band alignment; absolute deformation potential; biaxial strain; topological properties

1. Introduction

Thin-film heterojunction solar cells have become alternatives to traditional silicon-based ones due to superior properties.[1] $CuInSe_2$ is seen as a promising solar cell candidate with direct bandgap, high absorption and reduced component toxicity compared to other materials (CdTe, PbS, etc).[2] Buffer layer plays an important role in lattice adaptation, adhesion improvement and stress

relaxation between itself and the subsequent thin film[3]. A world-record efficiency of 22.3% has been achieved based on Cu(In,Ga)Se_2 absorber and CdS buffer[4]. Alternative buffer materials have been investigated for decades, primarily focusing on photo-generation, Cd replacement with environmentally friendly elements, and thermal stability adjustment.[5]

Bandgaps and band alignments are critical parameters for the design of solar cells. Bandgap determines a certain transparency at near-infrared spectrum, hence the degree of light absorption. Band alignments characterize the energy discontinuities in band edges, which serve as the basis for controlling transport properties and quantum confinement.[6] Buffer materials with satisfied band alignments and well-matched lattice parameters with absorber layers are essential.[7] Besides, the effect of epitaxial strain on electronic structures, absolute deformation potentials (ADPs)[8] and band alignments[9] should be focused on as well. Some progresses have been achieved in the calculation of these parameters from the first-principle theory. Vurgaftman et al[10] found that the total hydrostatic deformation potential is proportional to the pressure coefficient of direct bandgap. S. Kadantsev et al[8] found that the nonzero ADPs of reference core levels have reduced band offsets under compressive biaxial strain.

Figure 1a presents lattice constants and bandgaps of III-V and II-VI semiconductor compounds, as taken from reference.[6] Considering bandgaps and lattice matches, cost and environmental friendliness, "Cd-free" buffer material, AlP, has been suggested as suitable buffer material for its large bandgap and small lattice misfit with $CuInSe_2$ (less than 6%). Besides, AlP has higher refractive index than CdS, i.e. greater transmittance, in the range of [1.0;4.5] eV (**Figure 1b**), which contributes to the absorption degree of absorber layer. Meanwhile, when the photon energy *hf* is below 4.5 eV, $CuInSe_2$ has a higher absorption coefficient; when the photon energy *hf* is above 4.5 eV, AlP has a higher absorption coefficient (**Figure 1c**). The well-combined spectrum absorption of $CuInSe_2$/AlP heterostructure maximizes its whole optical ability. Until now, by contrast to other III-V compounds, AlP has not been studied as a buffer layer. In order to provide a foundation for its application, a comprehensive investigation of the properties of $CuInSe_2$/AlP heterostructure needs to be done.

In this work, heterostructures based on $CuInSe_2$ absorber with AlP buffer layer were modeled along [001] direction by using different stacking schemes and interfacial terminations. This direction was chosen as it corresponds to the smallest lattice mismatch (5.6%) between the two layers.

The interfacial distance d_0 and work of adhesion W_{ad} have been quantitatively examined to acquire a thermodynamically stable interface. Band alignments and ADPs of band energies as a function of (001) biaxial strain have been systematically computed. Recently, topological analyses of electron density based on the quantum theory of atoms in molecule (QTAIM)[11] have been used for interpreting interatomic interactions in real space for photovoltaic materials.[12] In combination with density of states, the stability and growth mechanism of heterostructure have been analyzed. Ultimately, the optical responses of heterostructures based on AlP and CdS buffer layers, as well as that of pure absorber have been estimated and compared as film thickness varies.

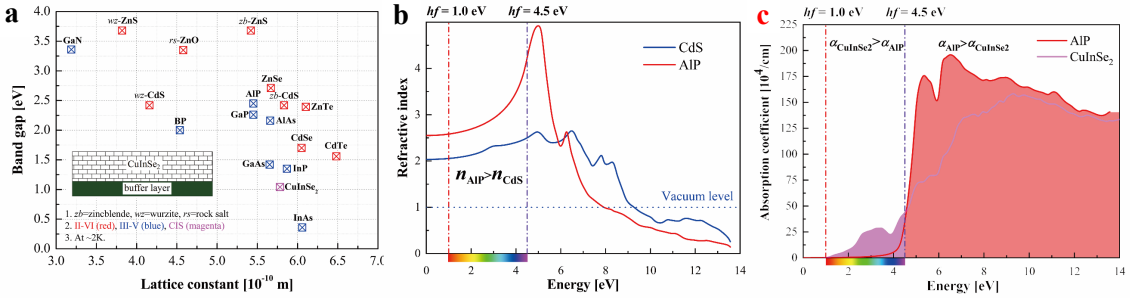

Figure 1. (a) Bandgaps and lattice constants of II-VI (red color), III-V (blue color) and $CuInSe_2$ (magenta) at ~2K, as taken from Ref.[6]. Abbreviations of "*zb*", "*wz*" and "*rs*" indicate zincblende, wurtzite, and rock salt crystal structures, respectively. Compounds without abbreviation crystallize in *zb* structure or related one (CIS). (b) Calculated refractive index of AlP and CdS and (c) absorption coefficient of AlP and $CuInSe_2$.

2. Computational details

First-principle calculations were carried out by full potential linear augmented plane wave method (FP-LAPW) as implemented in program WIEN2k.[13] The WC-GGA[14] functional has been used to describe exchange-correlation energy in structure optimizations. The convergence criteria on total energy, charge and force have been set to 10^{-5} Ry, 10^{-4} and 2 mRy/bohr, respectively. In order to improve the bandgap, which is underestimated with GGA functional, the modified Becke-Johnson exchange potential (mBJ) has been used. [15] The planewave cutoff parameter $R_{MT}K_{max}$ in the interstitial region was set to 7. A mesh of 1500 kpoints determined using the Monhkorst-Pack scheme was used to sample the Brillouin zone.

AlP and $CuInSe_2$ crystallize in cubic (space group *F*-43m) and tetragonal structures (space group *I*-42d), respectively, as shown in the inset of **Figure 2a** and **3a**. The heterostructures were

modeled using slabs composed of $(CuInSe_2)_m/(AlP)_n$ with a thickness of 15.0 Å vacuum layer. This vacuum layer was applied to separate free surfaces, avoiding interactions between periodic images. The lattice constant *m* and *n* correspond to the numbers of atomic layers in $CuInSe_2$ and AlP slabs, respectively. To meet the boundary condition and lattice coherence, the in-plane lattice constants (a and b) of heterostructure were both set to the mean value of bulk $CuInSe_2$ and AlP lattice constants. In such way, AlP side and $CuInSe_2$ side are under tensile and compressive strain respectively. The dependences of band edges on biaxial strain have been simulated as deformation ratios vary from -4% to 4% with respect to the equilibrium in-plane lattice constants *a* and b (with a=b) of $CuInSe_2$ and AlP, respectively. The chemical potential of each species in our model can be obtained by the first derivative of internal energy to particle number by neglecting the entropy and volume changes. Topological properties of electron density calculated in WIEN2k have been studied by program CRITIC2[16]. Spectroscopic limited maximum efficiency (SLME) has been valued as a useful indicator to characterize photovoltaic abilities.[17] In solar cell applications, conversion efficiency depends on the thickness of absorber layer.[18] The SLME of AlP- and CdS-based heterostructures, as well as pure $CuInSe_2$ thin film, have been calculated under AM 1.5G solar flux.

3. Surface investigations

The optimized lattice parameters (*a* and *c*), bulk moduli (*B*), bandgaps (*E*g) and elastic constants (C_{ij}) of $CuInSe_2$ and AlP, are listed in **Table 1**, together with the corresponding data taken from literature. The calculated lattice constants, bulk moduli and axial elastic constants with WC-GGA functional are well-matched to the literature data, whereas the shear modulus (C_{44} and C_{66}) of $CuInSe_2$ and the bandgaps of both $CuInSe_2$ and AlP are overestimated and underestimated, respectively. It is found that the bandgaps of $CuInSe_2$ and AlP have been improved by using the mBJ potential, which agree well with the experimental data. This validates our computational settings and the mBJ potential will be used hereafter.

Table 1. Calculated lattice parameters (*a* and *c*), bandgaps (*E*g), bulk moduli (*B*), and elastic constants (C_{ij}) of $CuInSe_2$ and AlP, together with corresponding data taken from literature.

Bulk		*a* (Å)	*c* (Å)	*E*g(eV)	*B* (GPa)	C_{ij} (GPa)					
						C_{11}	C_{12}	C_{13}	C_{33}	C_{44}	C_{66}
$CuInSe_2$	This work	5.786	11.606	0.22^{WC} 1.06^{mBJ}	73.7	94	61	67	83	109	118
	Calc.	5.782[a]	11.622[a]	-	-	71[b]	45[b]	45[b]	63[b]	46[b]	47[b]

		5.839[c]	11.734[c]	0.84[c]	64.4[c]	82[c]	55[c]	55[c]	81[c]	34[c]	-
	Exp.	5.781[d]	11.552[d]	1.02[d]	72.0[e]	97[d]	60[d]	86[d]	109[d]	36[d]	32[d]
AlP	This work	5.477	-	1.67[WC] 2.53[mBJ]	84.8	125	64	-	-	73	-
	Calc.	5.487[f]	-	1.73[f]	82.0[f]	125[f]	61[f]	-	-	63[f]	-
	Exp.	5.467[g]	-	2.52[g]	-	133[g]	63[g]	-	-	62[g]	-

[a]*Reference* [19]. [b]*Reference* [20]. [c]*Reference* [21]. [d]*Reference* [22].

[e]*Reference* [23]. [f]*Reference* [24]. [g]*Reference* [10].

AlP(001) slab with symmetric atomic layers were built to eliminate the spurious dipole effects. After full relaxation, the relative deviations of interlayer spacing with respect to bulk (Δd_{ij}) were calculated as N varies, as listed in **Table S1** (refer to the supplement information **Table S1**). The Δd_{ij} values at the middle layers have been used to determine the slab convergence, as plotted in **Figure 2a**. For low numbers of layers, Δd_{ij} decreases sharply as N increases. When N attains 13, the Δd_{ij} values tend to reach a plateau around 1% for two terminations. This 13-layers AlP(001) slab is thick enough to exhibit bulk-like interior, its surface energy σ can be written as:

$$\sigma = \frac{1}{2A_s}\left(E_{slab} - \sum_{x=Al,P} N_x \mu_x^{slab} - TS + PV\right) \quad (1)$$

where, E_{slab} is the slab energy, N_x and μ_x^{slab} are the numbers and chemical potentials of atoms in slab, respectively, and A_s is the surface area. P, V, T and S are the pressure, volume, temperature and entropy, respectively. Under atmospheric pressure, the products of TS and PV are zero at 0 K. As suggested in Ref.[25] the slab surface is in equilibrium with bulk, which means $\mu_{AlP}^{bulk} = \mu_{Al}^{slab} + \mu_P^{slab}$. Thus, equation (1) can be rewritten as:

$$\sigma = \frac{1}{2A_s}\left(E_{slab} + (N_P - N_{Al})\mu_{Al}^{slab} - N_P \mu_{AlP}^{bulk}\right) \quad (2)$$

With the aim to prevent the slab from breaking into energetically more stable substances, the chemical potential of atoms in the stabilized slab μ^{slab} should be lower than those in bulk phases μ^{bulk}. Following thermodynamics rules, μ_{AlP}^{bulk} equals to the sum of chemical potentials of atoms in bulk and an energetic term corresponding to compound formation energy (ΔG_f^0), reading $\mu_{AlP}^{bulk} = \mu_{Al}^{bulk} + \mu_P^{bulk} + \Delta G_f^0$. The formation energy $\Delta G_f^0(AlP)$ is approximated as the energy difference per formula $\Delta E_f^0(AlP)$ between Al, P and AlP. Thus, the chemical potential difference ($\mu_{Al}^{slab} - \mu_{Al}^{bulk}$) is in the range $[\Delta E_f^0; 0]$, being [-1.18;0] eV and [-1.21;0] eV for Al- and P-termination respectively.

The σ evolution of AlP(001) slab as a function of chemical difference ($\mu_{Al}^{slab} - \mu_{Al}^{bulk}$) can be obtained from equation (2), as soon as the chemical potentials of Al and AlP in bulk phases are

determined. As plotted in **Figure 2b**, the σ values of Al- and P-termination are in the ranges 1.06-1.37 J/m^2 and 1.17-1.50 J/m^2, respectively. Besides, there is a cross-point between them where chemical difference is -0.82 eV. Lower surface energy means larger stability.[26] In the ranges of [-1.21;-0.82] eV and [-0.82;0] eV, P- and Al-termination show opposite behaviors in evaluating the preferential surface stability.

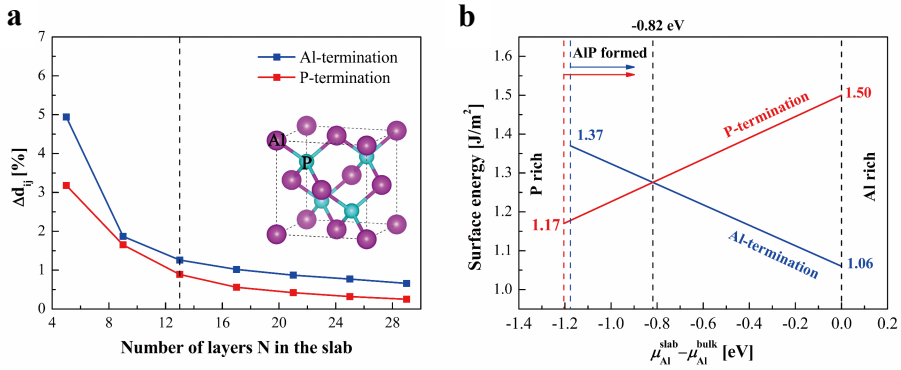

Figure 2. Relative deviations of interlayer spacing with respect to the number of atomic layers in AlP(001) slab for Al- and P-terminations (a) and their corresponding surface energies at 13-layers as a function of chemical difference ($\mu_{Al}^{slab} - \mu_{Al}^{bulk}$) (b). The inset of (a) shows AlP unit cell.

Similarly, the convergence tests of $CuInSe_2$(001) slabs, including Cu/In termination and Se termination (inset of **Figure 3a**), were conducted as well. After full relaxation, the interlayer spacing relative deviations with respect to bulk cannot be extracted precisely due to the great internal atomic displacements. Aiming to rapidly and accurately obtain the appropriate number of atomic layers, the incremental energy approach[27] was applied as the number of atomic layers N increases. The energy difference $E(N_j) - E(N_i)$ versus the increment of atomic layers $N_j - N_i$ was calculated, as plotted in **Figure 3a**. The energy difference first decreases and then keeps steady within an error range of 0.02 Ry. When atomic layers number reaches 13, the corresponding energy differences between 13-layers and 9-layers of Cu/In- and Se-terminated slabs are the lowest as well as the closest to the calculated bulk energy. Hence, a 13-layers slab has been considered thick enough to maintain a bulk-like interior. Note that the numbers of Cu atoms and In atoms are equal in the slab, i.e. $N_{Cu} = N_{In}$. Thus, its surface energy σ can be written as:

$$\sigma = \frac{1}{2A_s}\left(E_{slab} + \left(\frac{1}{2}N_{Se} - N_{Cu}\right) \times \left(\mu_{Cu}^{slab} + \mu_{In}^{slab}\right) - \frac{1}{2}N_{Se}\mu_{CuInSe_2}^{bulk}\right) \quad (3)$$

Similarly, the 0 K formation energy ΔE_f^0 of $CuInSe_2$ can be obtained through the energy difference per formula between Cu, In, Se and $CuInSe_2$, which is -1.80 eV for two terminations. The chemical difference of $(\mu_{Cu}^{slab} - \mu_{Cu}^{bulk} + \mu_{In}^{slab} - \mu_{In}^{bulk})$ is in the range $[2\Delta E_f^0; 0]$. The σ evolution as a function of chemical difference can be deduced from equation (3), as soon as the chemical potentials of Cu, In and $CuInSe_2$ in bulk phases are determined. As plotted in **Figure 3b**, the σ values of Cu/In- and Se-termination are in the ranges 0.84-1.70 J/m^2 and 0.16-1.02 J/m^2, respectively. There is also a cross-point where chemical difference is -0.38 eV. Se-termination and Cu/In-termination behave reversely in seeking for favorable stability in the ranges of [-3.60;-0.38] eV and [-0.38;0] eV. Therefore, both Al- and P-terminated AlP surfaces together with Cu/In- and Se-terminated $CuInSe_2$ surfaces need to be considered in the forthcoming heterostructure modeling.

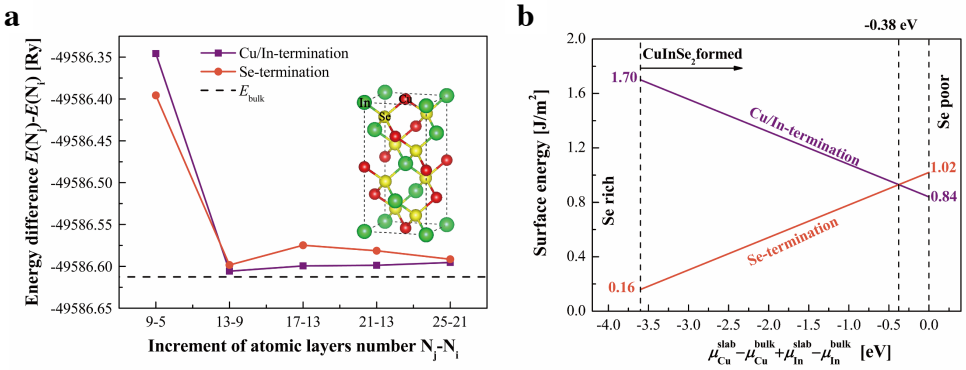

Figure 3. Energy difference $E(N_j) - E(N_i)$ versus the increment of atomic layers number $N_j - N_i$ in $CuInSe_2$(001) slab for Cu/In- and P-terminations (a) and their corresponding surface energies at 13-layers as a function of chemical difference $(\mu_{Cu}^{slab} - \mu_{Cu}^{bulk} + \mu_{In}^{slab} - \mu_{In}^{bulk})$ (b). The inset of (a) shows $CuInSe_2$ unit cell.

4. Interface investigations

4.1 Interface modeling and surface adhesion

The $CuInSe_2$/AlP heterostructures with two types of interfacial bondings, i.e. Se-Al and Cu/In-P, were modeled based on the above convergence tests. In effect, since the adjacent layers share neither common anion nor cation, these interfacial bondings unnecessarily lead to the same band offsets.[28] Three stacking schemes for each interfacial termination, designated as "stack1", "stack2" and "stack3", are under consideration. As presented in **Figure 4**, "stack1", "stack2" and "stack3" means that atoms from the first atomic layer of $CuInSe_2$(001) slab sit at the "diagonal" midpoint,

at the "lateral" midpoint and directly "on-top" of atoms from the first atomic layer of AlP(001) slab, respectively. Hereafter, the (001) plane index of $CuInSe_2$ and AlP will be omitted for simplification. The work of adhesion, W_{ad}, as characterized by the energy difference between separate slabs and their combined heterostructure, has been used to portray the heterointerface properties, such as strength and stability. The W_{ad} of $CuInSe_2$/AlP is given by,[25]

$$W_{ad}(CuInSe_2/AlP) = \left(\sum_X E^{slab}_{X=CuInSe_2,AlP} - E^{hetero}_{CuInSe_2/AlP}\right)/A_i \quad (4)$$

where, E^{slab}_X is the fully relaxed slab energy, and $E^{hetero}_{CuInSe_2/AlP}$ is the heterostructure energy and A_i is the interfacial area.

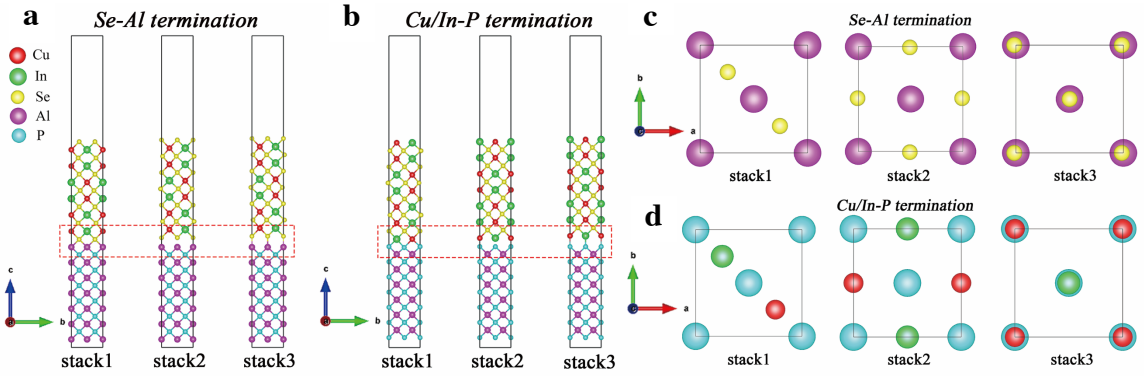

Figure 4. Stacking schemes of $CuInSe_2$/AlP heterostructures: (a) Se-Al termination; (b) Cu/In-P termination. "stack1", "stack2", and "stack3" represent "diagonal" midpoint, "lateral" midpoint, and "on-top" stacking as depicted in (c) for Se-Al termination and (d) for Cu/In-P one.

The W_{ad} was investigated by the universal binding energy relation (UBER)[29] method. By calculating a series of unrelaxed supercells with different interfacial distances d_0, the W_{ad} of each model can be drawn, as shown in **Figure 5**. After smoothing the W_{ad}-d_0 curves, the optimal d_0 and its corresponding W_{ad} can be determined from the vertex of each curve, as listed in **Table 2**. For both two terminations, the maximum values of W_{ad} for different stacking schemes follow the order W_{ad}(stack3)>W_{ad}(stack1)>W_{ad}(stack2). "On-top" stacking at the optimal interfacial distance is the most thermodynamically stable, with the highest W_{ad} of 4.405 J/m^2 and 4.467 J/m^2 for Se-Al and Cu/In-P terminations respectively. Besides, a considerable difference in W_{ad} between Se-Al-stack1 and Cu/In-P-stack1 is observed in comparison with that of -stack2 and -stack3, for which the optimal d_0 and corresponding maximum W_{ad} are both well-matched between the two terminations.

At the optimal interfacial distance, heterostructures have been relaxed until the total residual forces on each atom were less than 2 mRy/Bohr. For the sake of time- and cost-saving, only the

four atomic layers near interface (enclosed within the red dash lines in **Figure 4a** and **4b**) have been considered. As shown in **Table 2**, the work of adhesion after relaxation still follows the same order as the one generated from UBER. As discussed before, the maximum surface energies of Al- and P-terminated AlP slabs can reach up to 1.37 J/m^2 and 1.50 J/m^2, respectively. Correspondingly, their work of adhesion W_{ad}(AlP/AlP) along [001] direction can be obtained according to equation (4), i.e. 2.74 J/m^2 and 3.00 J/m^2 respectively, which are twice the surface energies since the interfacial energy of the "AlP/AlP heterostructure" is viewed as zero. In the thermodynamic system, substrate with sufficient interfacial stability is indispensable for heterogeneous nucleation. Compared to W_{ad}(AlP/AlP), the W_{ad} of Se-Al-stack3 and Cu/In-P-stack3 heterostructures are larger, which means that $CuInSe_2$ thin film is more likely to form on AlP substrate than AlP itself.

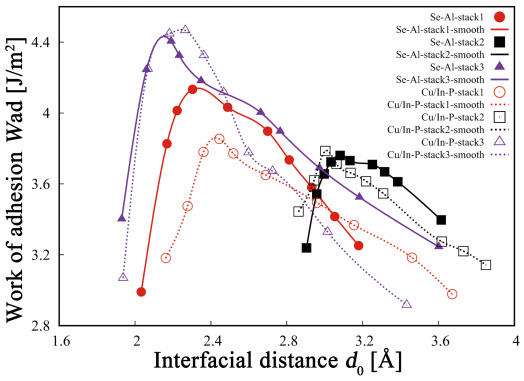

Figure 5. Work of adhesion W_{ad} *vs*. interfacial distance d_0 of Se-Al (solid symbols) and Cu/In-P (hollow symbols) terminations for each stacking. Solid and dash lines are their smoothing curves. Color code : stack 1 in red, stack 2 in black, stack 3 in purple.

Table 2. Optimal interfacial distance d_0 with corresponding W_{ad} obtained from smoothing curves in **Figure 5**, as well as the W_{ad} after relaxation.

Interfacial terminations	Stacking schemes	UBER		Relaxed_W_{ad} (J/m^2)
		d_0 (Å)	W_{ad} (J/m^2)	
Se-Al	stack1	2.303	4.131	3.816
	stack2	3.081	3.761	3.756
	stack3	2.190	4.405	4.408
Cu/In-P	stack1	2.444	3.854	3.650
	stack2	3.003	3.837	3.479
	stack3	2.265	4.467	4.629

4.2 Band alignment

The valence band offset ΔE_v is calculated following the same procedure as that in core-level photoemission measurement,[30] which is defined as:

$$\Delta E_v(CuInSe_2/AlP) = \Delta E_{VBM,C}^{CuInSe_2} - \Delta E_{VBM,C'}^{AlP} + \Delta E_{C,C'} \quad (5)$$

where, $\Delta E_{VBM,C}^{CuInSe_2}$ and $\Delta E_{VBM,C'}^{AlP}$ are energy separations between core level and valence band maximum of bulk $CuInSe_2$ and AlP, respectively, and $\Delta E_{C,C'}$ is the difference in core level binding energies between cations and anions at interface. The average core level of cations and anions at interface is chosen as the reference core level, E_{ref}. For Se-Al interfacial termination, Al 1s and Se 1s are assigned as cation and anion core states respectively. For Cu/In-P interfacial termination, 1/2(Cu 1s+In 1s) and P 1*s* are set as cation and anion core states respectively. Besides, the conduction band offset ΔE_c can be obtained by $\Delta E_c = \Delta E_g + \Delta E_v$, where ΔE_g is the calculated bandgap difference between bulk $CuInSe_2$ and AlP.

Table 3 lists the energy separations from E_{ref} to VBM, core level binding energy differences $\Delta E_{C,C'}$, natural band offsets and corresponding types of $CuInSe_2$/AlP heterostructures. Core level binding energy difference is correlated with band alignment; the greater value of $\Delta E_{C,C'}$, the larger value of ΔE_v. Se-Al-stack1 and -stack3 heterostructures have type-I ("spike-like") band offsets, where both CBM and VBM belong to $CuInSe_2$; Se-Al-stack2 has type-II ("cliff-like") band offset, where CBM and VBM belong to AlP and $CuInSe_2$, respectively. Besides, Cu/In-P-stack1, -stack2 and -stack3 heterostructures all have type-I ("spike-like") band offsets. Regardless of the types of terminations, their absolute values of $\Delta E_{C,C'}$ at interface follow the order stack3>stack1>stack2, which is surprisingly in accordance with their work of adhesions.

Table 3. Energy separations (Ry) from core level to VBM of bulk $CuInSe_2$ and AlP, core level binding energy differences (Ry), band offsets (eV) and corresponding types of $CuInSe_2$/AlP heterostructures.

$CuInSe_2/AlP$ heterostructures	Se-Al termination			Cu/In-P termination		
	stack1	stack2	stack3	stack1	stack2	stack3
$\Delta E_{VBM,C}^{CuInSe_2}$		918.2201			1344.0435	
$\Delta E_{VBM,C'}^{AlP}$		110.5463			152.5341	
$\Delta E_{C,C'}$	-807.5684	-807.5554	-807.5742	-1191.4516	-1191.4119	-1191.4683
$\Delta E_v(CuInSe_2/AlP)$	1.434	1.608	1.355	0.786	1.326	0.559
$\Delta E_c(CuInSe_2/AlP)$	0.035	-0.139	0.114	0.683	0.143	0.910
Type	I	II	I	I	I	I
$\Delta E_v^{re}(CuInSe_2/AlP)$	1.528	1.702	1.449	0.920	1.460	0.693
$\Delta E_c^{re}(CuInSe_2/AlP)$	-0.067	-0.241	0.012	0.590	0.050	0.817
Type^{re}	II	II	I	I	I	I

** ΔE_v^{re}, ΔE_c^{re} and type^{re} represent the revised valence and conduction band offsets and corresponding types of heterostructures when considering the ADPs of band energies under biaxial strain. These results will be discussed in the next section.*

During the electron transition process in photovoltaic devices, effective transportation should happen before the excited electrons recombine or fall back into a lower energy level. $CuInSe_2$/AlP interface is characterized by high defect formation mainly due to the lattice and thermal expansion mismatches[31,32]. These defects play a fundamental role in solar cell performance. The heterointerface should exhibit minimum recombination and current loss thus allowing for the maximum open-circuit voltage. According to Courel et al.[33], interfacial recombination depends on the combining velocity and minority carriers concentration, defined as follow:

$$J_{inter} = qSn_{i-CuInSe_2}\left(1 + \gamma_{DOS}e^{-(\Delta E_v + \Delta E_c)/2kT}\right) \quad (6)$$

where, J_{inter} is the reverse saturation current density due to recombination, q is electron charge, S is recombination velocity, γ_{DOS} is density of states enhancement factor between $CuInSe_2$ and AlP.

So, the influence of band offsets on minority carrier recombination can be demonstrated. Indeed, "spike-like" heterojunction (ΔE_c>0) has less interfacial recombination than "cliff-like" one (ΔE_c<0). Interface owning positive CBO bears more favorable carrier transportation properties than that owning negative one. However, large CBO is viewed as a sufficiently high barrier so that majority of electrons generated in the absorber layer will recombine before passing through. This electron-hole recombination at the absorber surface is detrimental to open-circuit voltage. Besides, small VBO causes significant electron confinement without hindering the hole injection in a light-emitting device.[34] This will increase the chance of recombination as well. Thus, band offsets should be strictly limited in a certain range. Though Cu/In-P-stack3 has slightly larger interfacial stability than Se-Al-stack3, its large CBO and small VBO greatly deteriorate the performances regarding band lineup and external quantum efficiency.

4.3 Absolute deformation potentials (ADPs) under biaxial strain

In the above calculations, there is a basic assumption that the absolute core level deformation potential is zero, therefore the band alignment between solids is intrinsic. However, there is a great uncertainty on deformation potentials, which comes from the strain effects in pseudo-morphically grown layers.[8] To precisely predict band offsets, the ADPs of energy bands, accounting for band edges and core levels, have been considered in the following calculations. The average in-plane lattice constant at interface results in compressive strain at $CuInSe_2$ slab and tensile strain at AlP

one. For a given deformation ratio, their optimized out-of-plane lattice constants and volumes were obtained (refer to supplement information **Figure S1**). As proposed in Ref.[8], the change in band energy under biaxial strain is defined as a_V^{band}. The ADP of VBM can be expressed as $a_V^{VBM} = a_V^{VBM/1s} + a_V^{1s}$, where $a_V^{VBM/1s}$ is the deformation potential of VBM with respect to E_{ref}, and a_V^{1s} is the reference core level and was determined in the previous natural band offsets calculation.

Figure 6 shows the biaxial strain-modified band energies, including CBM, VBM and core levels, of bulk AlP and $CuInSe_2$. As strain goes from compressive to tensile, the band energies decrease continuously, which gives negative ADPs. The nonnegligible ADPs, when subjected to biaxial strains, emphasize the importance of controlling lattice mismatch between thin film and substrate. By fitting band energies to the polynomial of third-degree, the ADPs can be determined from the first derivative of the fitted curves with respect to volume. The a_V^{VBM}, a_V^{CBM} of AlP and $CuInSe_2$ at the average in-plane lattice constant (marked as "*" in **Figure 6**) are -82.4 meV/Å^3, -100.9 meV/Å^3 and -39.2 meV/Å^3, -20.4 meV/Å^3, respectively. Taking the core level deformation potential into account, the $a_V^{VBM/1s}$ of AlP and $CuInSe_2$ are -0.3 meV/Å^3 and -10.2 meV/Å^3, respectively. AlP has an equivalent variation of core level and valence band edge when subjected to strain. This strong resistance against strain contributes to its potentiality in buffer layer applications. By contrast, $CuInSe_2$ has an unbalanced variation of core level and valence band edge.

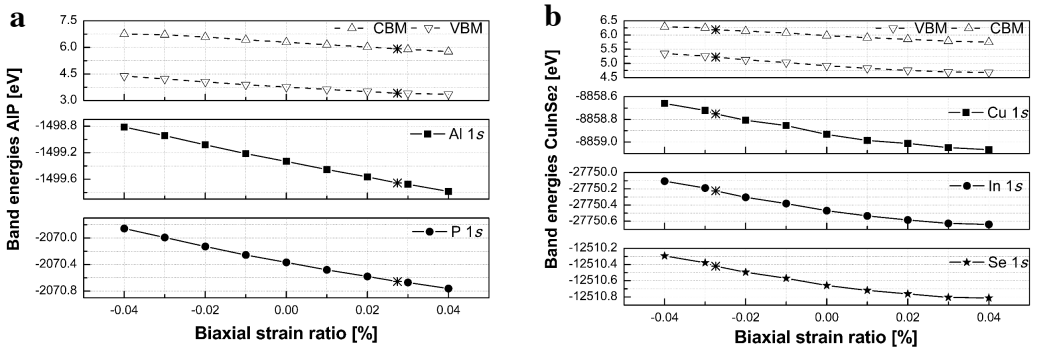

Figure 6. Evolution of band energies, for VBM, CBM and core levels of bulk AlP (a) and $CuInSe_2$ (b) as biaxial strain ratio varies. The star symbol "*" shows the average lattice constant ratio.

At the average lattice constant, the absolute band energies can be given by the product of ADPs and volume deformation. Associating the biaxial strain modified CBM and VBM with the reference core levels and equation (5), the revised VBO ΔE_v^{re} and CBO ΔE_c^{re} can be expressed as:

$$\Delta E_{v(c)}^{re} = \Delta E_{v(c)} + a_V^{V(C)BM} \mathrm{d}V(\mathrm{CuInSe_2}) - a_V^{V(C)BM} \mathrm{d}V(\mathrm{AlP}) \quad (7)$$

where, $\Delta E_{v(c)}$ is the natural valence and conduction band offsets obtained previously without considering band energy deformation. The revised band offsets are listed in **Table 3**, marked by "re". Regarding Se-Al termination, for a given raw band offset, the revised VBO has increased by 94.0 meV, as a result of the energy upshift of VBM towards core level in $CuInSe_2$ which amounts to 93.1 meV, and the negligible energy downshift of -0.9 meV in AlP. The revised CBO has decreased by 102.3 meV due to the large downshift of CBM towards VBM in $CuInSe_2$, which is -171.4 meV, coupled with a small downshift of -69.1 meV in AlP. The revised VBO and CBO for Cu/In-P heterostructure termination can be obtained as well as soon as the energy shifts between VBM, CBM and core level are determined.

Figure 7 depicts the schematic diagram of revised band offsets. Se-Al-stack1 heterostructure has been changed from type-I into type-II due to ADP correction. Se-Al-stack3 and Cu/In-P-stack3, as the most stable heterostructures, have revised CBOs of 12 meV and 817 meV respectively. The nearly flat "spike-like" CBO of Se-Al-stack3 will boost open-circuit voltage and electron transition, as suggested in Ref.[35,36]. Accordingly, the considerable "spike-like" CBO of Cu/In-P-stack3 shall constrain its interest in heterostructure assessment, since CBO is recognized as the depth of quasiparticle confinement. As mentioned in Ref.[37], the discrepancy in strain states between two neighboring heterointerfaces is directly correlated to the asymmetric charge distribution feature. Electrons released from the $CuInSe_2$ absorber layer are supposed to cross the barrier in the short term before getting recombined or degenerated. In view of that, Se-Al-stack3 heterostructure has become our best choice due to its favorable band lineup. Furthermore, its thorough investigations on strain modified band edges provide us perspectives on choosing and determining appropriate buffer layer in thin film manufacturing. These strain-mediated evolutions of band edges could offer additional degrees of freedom for achieving the desired functionality and utility.

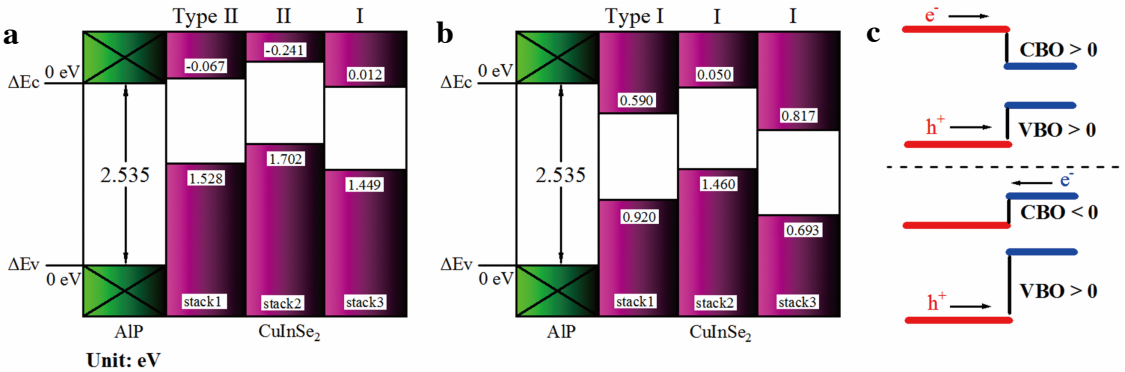

Figure 7. Schematic diagram of revised band offsets and corresponding types of Se-Al termination (a) and Cu/In-P termination (b) of $CuInSe_2$/AlP heterostructures, and illustration of the migration of electrons and holes at the type-I and type-II heterointerfaces (c).

4.4 Electronic density topological properties and density of states (DOS)

To further unravel the influence of terminations and stacking schemes on interfacial properties, the topological properties of electron density ϱ as well as the Laplacian $\nabla^2\rho$ distribution have been investigated as shown in **Figure S2**. Se-Al-stack3 and Cu/In-P-stack3 have been chosen as the representatives for each type of termination. Their atomic arrangements near interfaces, electron density and Laplacian in the plane (-110) are shown in **Figure 8a-c** and **8e-g,** respectively. The symbols "b", "r" and "c" represent bond, ring, and cage critical points as defined in QTAIM theory.[11] According to the local virial theorem, the relation between Laplacian, kinetic G_{BCP} and potential V_{BCP} energy densities can be defined as $\hbar^2/4m\,\nabla^2\rho_{BCP} = 2G_{BCP} + V_{BCP}$[38], where BCP stands for bond critical point. A perfect heterointerface state is supposed to form Cu-Se, In-Se, Al-P, and Al-Se interactions for Se-Al termination and Cu-Se, In-Se, Al-P, Cu-P and In-P interactions for Cu/In-P termination. Espinosa et al.[39] used $|V_{BCP}|/G_{BCP}$ ratio and introduced bond degree (BD=H_{BCP}/ϱ_{BCP}) to distinguish bond types. As depicted in **Figure 8d** and **8h**, the bond degrees of all pairwises are in the range of 1 to 2. This means that their interatomic interactions lie in *transit* closed-shell zone, showing metal-covalent behaviors, between the typical ionic and covalent bonds.

Total and partial density of states (DOS) near the interface have been plotted as well (insets of **Figure 8d** and **8h**). The atomic orbital contributions near Fermi level can be obtained. All the orbitals show large overlaps, leading to a metallic-like interface. The bonding between Al and P has been divided into Al-P and Al-P* to feature their dissemblance in bond length. The asterisk sign "*" indicates the longer one. As seen in **Figure 8d**, the absolute magnitude of BD for each pairwise at Se-Al-stack3 interface complies with the following sequence, In-Se>Al-P>Al-P*>Cu-Se>Al-Se. According to the DOS, Cu d- and Se/Al/P p-orbitals contribute the most to the interfacial orbital composition. Pairwise In-Se has the largest bond degree, but its atomic contribution to DOS is weak due to the negligible In p-orbital contribution near Fermi level. Hence, Cu-Se, Al-P, and Al-Se are the main bonding pairwises to focus on in relation to interfacial properties. The "p-p" overlap of pairwise Al-P forms a strong covalent chemical bond in AlP slab. The similar BD of Al-P and Al-P* indicates a uniform interfacial chemical characteristic at AlP side. At $CuInSe_2$ side, there is a strong "p-d" overlap of pairwise Cu-Se. Its high atomic orbitals contribution and small

$|V_{BCP}|/G_{BCP}$ ratio imply a reactive and delocalized bonding. At the heterointerface of $CuInSe_2$/AlP, the bond degree of pairwise Al-Se is -0.272 kJ/mol per electron. This established covalent bonding acknowledges the chemical feasibility of utilizing AlP as a buffer layer.

At the Cu/In-P-stack3 interface (**Figure 8f** and **8g)** there is no bond critical point between In and P atoms. This could be a result of the large displacement of In atoms from their bulk positions during relaxation. Therefore, the interior strain cannot be ignored. The absolute magnitude of BDs for each pairwise follows the order Cu-P>In-Se>Al-P>Cu-Se>Al-P*. The interfacial behavior can be delineated in the light of interatomic interactions. Pairwise Cu-P owns the biggest absolute BD of 0.497 kJ/mol per electron, i.e. the strongest interatomic interaction. It implies that Cu atom can easily dispose atop P atom. Besides, as the inset of **Figure 8h** shows, the density of states near Fermi level is mainly composed of Cu d-orbitals and P p-orbitals. This could explain the largest interfacial stability of Cu/In-P-stack3 heterostructure. Pairwise Al-P and Al-P* characteristics differ more significantly than those in Se-Al-stack3. This is in line with the obvious inequalities in density of states contribution between In and Cu atoms.

In addition, the band edges of $CuInSe_2$ are based on the bonding and antibonding states. The absolute position of VBM and thus chemical trends are strongly dependent on the coupling between d and p states.[40] The optical bandgap is associated with the repulsion between Cu d and Se p valence band states in $CuInSe_2$. That is, as the Se p-orbitals combine with the Cu d-orbitals, the VBM of $CuInSe_2$ shifts upward, corresponding to p-d repulsion.[41] As a result, a narrowing bandgap can be established, which is consistent with the result in **Figure 6b**. Hence, as a result of the strong mixing of "Cu d-Se p" of Se-Al-stack3 heterostructure discussed above, large VBO and thus small CBO are obtained. Similarly, the weak contribution of Se p-orbitals at Cu/In-P-stack3 interface, as the inset of **Figure 8h** shows, results in a small VBO and thus large CBO. These assessments are in accordance with the findings shown in **Figure 7**.

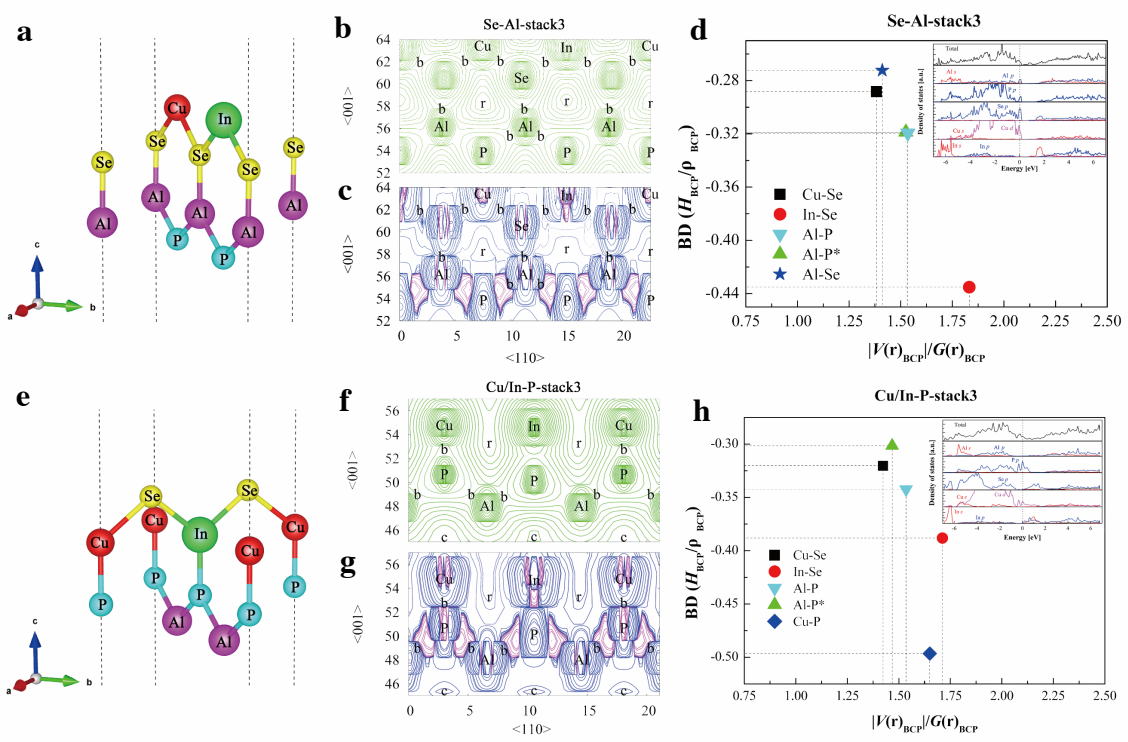

Figure 8. Schematic diagrams of Se-Al-stack3 (a) and Cu/In-P-stack3 (e) near the interface, and their electron density ϱ (b and f), electron density Laplacian $\nabla^2\rho$ (c and g), and bond degree (BD=H_{BCP}/ϱ_{BCP}) *vs*. $|V_{BCP}|/G_{BCP}$ (d and h) at BCPs in the plane (-110). The asterisk sign (*) stands for the longer bond length for pairwise Al-P. The insets in (d) and (h) show total and partial density of states of atoms near interface.

4.5 Spectroscopic limited maximum efficiency SLME

According to Crovetto and Hansen[42], low-efficiency cells have large "cliff-like" offsets, whereas most high-efficiency cells have "spike-like" or nearly flat offsets. According to the preceding discussions, the "on-top" stacking terminated as Se-Al at interface is foreseen as the most promising heterostructure. To better characterize both the designated "absorber-buffer" heterojunction and the pure $CuInSe_2$ absorber their photovoltaic responses have been calculated. In addition to the AlP-based heterostructure, a CdS-based one has been modeled with the same interfacial condition for the purpose of comparison. By computing the absorption coefficient in [280;1200] nm wavelength range (blue curve in **Figure 9b**), the short circuit current J_{SC}, open-circuit voltage V_{OC} and conversion efficiency with respect to thickness were obtained, as shown in **Figure 9**.

There is a prerequisite that the buffer layer is thin enough for electrons generated by absorber to tunnel through in view of the favorable band lineup. As shown in **Figure 9a**, the short circuit current increases significantly as film thickness increases, which is mainly due to the enriched carrier capacity. Meanwhile, the open-circuit voltage decreases slightly as film thickness increases, which signifies the occurrence of carrier recombinations at interfaces and interiors. Heterostructure has a lower current density than pure $CuInSe_2$ at the same thickness, showing a sharper and narrower current-voltage contour. This might come from the increased series resistance when AlP and CdS serve as buffer layers. As seen from **Figure 9b**, the maximum efficiencies of heterostructures and pure $CuInSe_2$ increase rapidly at the early stage and then tend towards the converged value. It is found that 0.3 μm $CuInSe_2$ absorber is seen as thick enough to attain a converged efficiency of 27.42%, which is close to the results of Ref.[43,44] under the same condition. Similarly, 0.5 μm Se-Al-stack3 and Cd-Al-stack3 heterostructures have attained their converged efficiencies, 27.39% and 27.41%, respectively. These two heterostructures possess not only high (close to pure $CuInSe_2$ absorber) but also similar optical properties. In other words, AlP can be utilized as a promising alternative in buffer material in pursuing high efficiency and low-cost solar cell. Therefore, the addition of AlP buffer merely affects the whole scale of optical properties, which undoubtfully, benefits from the well-matched interface condition, as illustrated before.

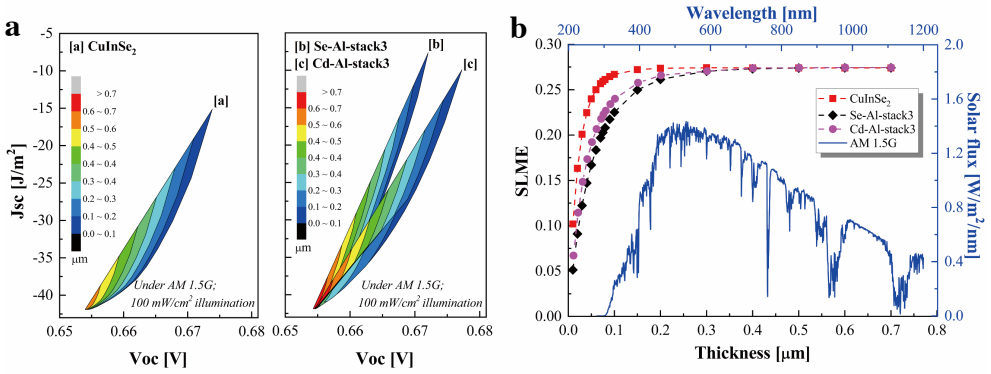

Figure 9. Calculated *J*sc-*V*oc characteristics (a) and spectroscopic limited maximum efficiency (b) with respect to the thickness of Se-Al-stack3 and Cd-Al-stack3 heterostructures and pure $CuInSe_2$ under AM 1.5G, namely 100 mW/cm² illumination. The range of light absorption wavelength is 280 nm-1200 nm.

5. Conclusions

In this work, we have chosen the AlP compound as a buffer layer for $CuInSe_2$ thin film. The $CuInSe_2$/AlP heterostructures have been modeled by different stacking schemes and interfacial terminations. The optimal interfacial distance, thermodynamic stability and band alignment have been computed. Heterointerface at "on-top" stacking is the most thermodynamically stable compared with other stackings. There is a correlation between band alignments and core level binding energy difference at the heterointerface. The biaxial strain-induced deformation of band energies and hence their absolute deformation potentials have been determined. The revised valence and conduction band offsets of $CuInSe_2$/AlP heterostructure have increased and decreased, respectively. Both Se-Al and Cu/In-P "on-top" stackings has "spike-like" band offsets, and the former has flat CBO, 12 meV. Topological analysis of electron density unveils interatomic interactions at heterointerfaces and provides insightful information for material manufacturing. The strong mixing between Cu d and Se p states plays a decisive role in defining the absolute position of valence band maximum and thus the chemical trends. The SLME studies reveal that $CuInSe_2$/AlP heterostructure can attain 27.39% of efficiency, which is similar to that of CdS-based heterostructure. This provides a solid basis for AlP as buffer layers in future applications.

6. Supporting information

The following files are available free of charge.

Table S1. AlP(001) surface relaxation of the two types of terminations as a function of the number of layers N in the slab, Δd_{ij} is the change of interlayer distance in the percentage of bulk spacing.

Termination	Change in interlayer	Number of layers N in the slab						
		5(%)	9(%)	13(%)	17(%)	21(%)	25(%)	29(%)
Al-	Δd_{12}	4.93	5.42	4.72	4.54	4.16	3.98	3.88
	Δd_{23}	4.94	2.72	2.15	1.94	1.62	1.44	1.37
	Δd_{34}		1.41	0.87	0.63	0.28	0.17	0.07
	Δd_{45}		1.87	1.08	0.80	0.56	0.35	0.27
	Δd_{56}			1.40	1.12	0.84	0.74	0.62
	Δd_{67}			1.26	1.04	0.84	0.63	0.54
	Δd_{78}				1.04	0.84	0.67	0.58
	Δd_{89}				1.02	0.94	0.74	0.62
	Δd_{910}					0.87	0.74	0.62
	Δd_{1011}					0.87	0.74	0.66
	Δd_{1112}						0.74	0.66
	Δd_{1213}						0.77	0.66
								0.70

								0.66
	Δd_{12}	-1.11	-1.75	-1.49	-3.18	-2.28	-2.38	-2.52
	Δd_{23}	3.18	3.28	3.30	3.16	3.09	3.02	2.99
	Δd_{34}		0.11	-0.96	-1.37	-1.51	-1.65	-1.70
	Δd_{45}		1.65	1.81	1.64	1.54	1.47	1.43
	Δd_{56}			0.47	0.10	-0.05	-0.14	-0.17
	Δd_{67}			0.89	0.77	0.67	0.56	0.53
	Δd_{78}				0.39	0.23	0.14	0.10
P-	Δd_{89}				0.56	0.51	0.42	0.33
	Δd_{910}					0.36	0.25	0.18
	Δd_{1011}					0.42	0.35	0.29
	Δd_{1112}						0.28	0.25
	Δd_{1213}						0.32	0.25
								0.25
								0.25

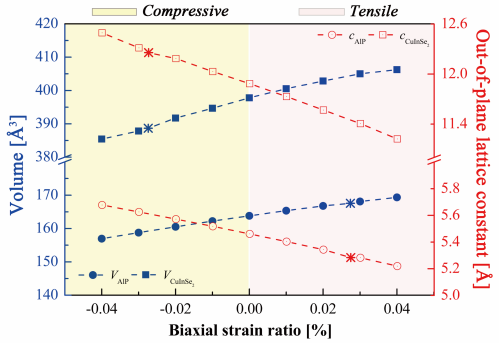

Figure S1. Calculation of the conventional cells in out-of-plane lattice constant and volume of AlP and $CuInSe_2$ as a function of biaxial strain ratio in [-4%;4%].

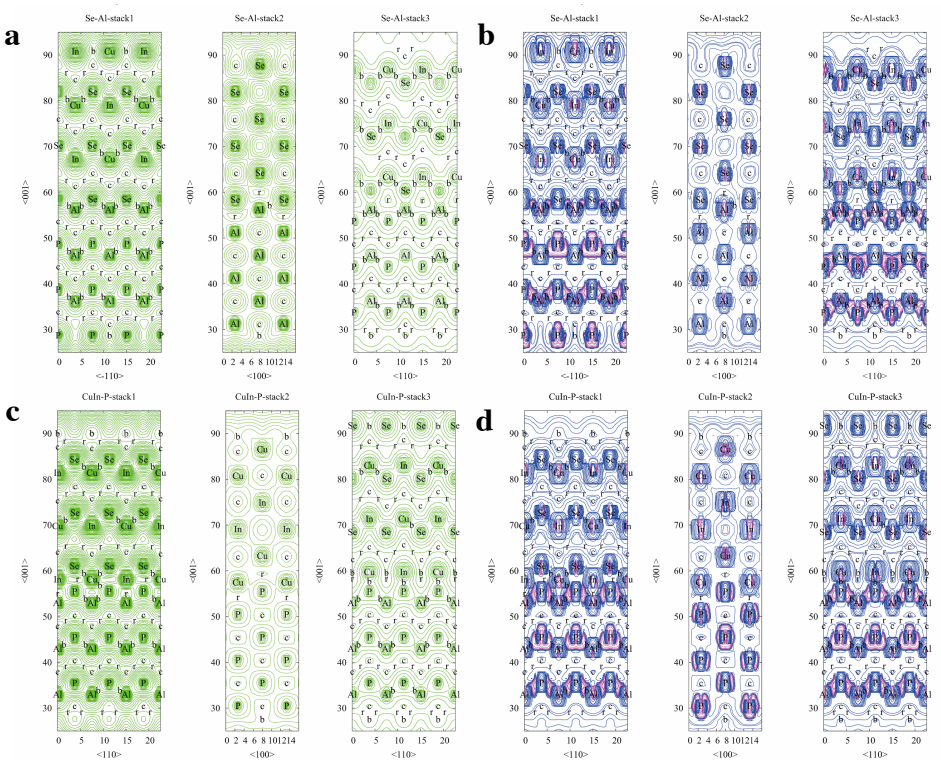

Figure S2. Topological properties of Se-Al terminated and Cu/In-P terminated heterostructure: electron density (a and c) and electron density Laplacian (b and d).

7. Author information

Corresponding Author

*E-mail: m-c.record@univ-amu.fr.

8. Acknowledgments

This work is financially supported by the China Scholarship Council (CSC). This work was granted access to the HPC resources of the Centre Informatique National de l'Enseignement Supérieur (CINES), Montpellier, France under allocation A0050806881 made by the Grand Equipement National de Calcul Intensif (GENCI). It was also granted access to the HPC resources of Aix-Marseille Université financed by the project Equip@Meso (ANR-10-EQPX-29-01) of the program "Investissements d'Avenir" supervised by the Agence Nationale de la Recherche.

9. References

1 M. A. Green, *J Mater Sci: Mater Electron*, 2007, **18**, 15–19.
2 Md. A. Hossain, M. Wang and K.-L. Choy, *ACS Appl. Mater. Interfaces*, 2015, **7**, 22497–22503.
3 K. Mokurala, L. L. Baranowski, F. W. de Souza Lucas, S. Siol, M. F. A. M. van Hest, S. Mallick, P. Bhargava and A. Zakutayev, *ACS Comb. Sci.*, 2016, **18**, 583–589.

4 2015, http://www.solar-frontier.com/eng/news/2015/C051171.html, (accessed November 15, 2019).
5 J.-H. Wi, W.-J. Lee, D.-H. Cho, W. S. Han, J. H. Yun and Y.-D. Chung, *physica status solidi (a)*, 2014, **211**, 2172–2176.
6 S. M. Sze and K. K. Ng, *Physics of semiconductor devices*, John Wiley & Sons, New Jersey, 3rd edition., 2007.
7 Y. Z. Hamri, Y. Bourezig, M. Medles, M. Ameri, K. Toumi, I. Ameri, Y. Al-Douri and C. H. Voon, *Solar Energy*, 2019, **178**, 150–156.
8 E. S. Kadantsev and P. Hawrylak, *Applied Physics Letters*, 2011, **98**, 023108.
9 Y.-H. Li, A. Walsh, S. Chen, W.-J. Yin, J.-H. Yang, J. Li, J. L. F. Da Silva, X. G. Gong and S.-H. Wei, *Applied Physics Letters*, 2009, **94**, 212109.
10 I. Vurgaftman, J. R. Meyer and L. R. Ram-Mohan, *Journal of Applied Physics*, 2001, **89**, 5815–5875.
11 R. F. W. Bader, *Atoms in molecules: a quantum theory*, Clarendon Press, Oxford, 1990.
12 P. Jiang, P. Boulet and M.-C. Record, *J. Mater. Chem. C*, 2019, **7** , 5803–5815.
13 P. Blaha, K. Schwarz, G. K. H. Madsen, D. Kvasnicka and J. Luitz, *WIEN2k, an augmented plane wave+local orbitals program for calculating crystal properties Karlheinz Schwarz, Techn. Universität Wien, Austria*, 2001.
14 Z. Wu and R. E. Cohen, *Phys. Rev. B*, 2006, **73**, 235116.
15 F. Tran and P. Blaha, *Phys. Rev. Lett.*, 2009, **102**, 226401.
16 A. Otero-de-la-Roza, E. R. Johnson and V. Luaña, *Computer Physics Communications*, 2014, **185**, 1007–1018.
17 L. Yu and A. Zunger, *Physical Review Letters*, 2012, **108**, 068701.
18 W. Yin, T. Shi and Y. Yan, *Advanced Materials*, 2014, **26**, 4653–4658.
19 J. Parkes, R. D. Tomlinson and M. J. Hampshire, *Journal of Applied Crystallography*, 1973, **6**, 414–416.
20 M. S. and I. Alhayek, in *Advances in Composite Materials - Ecodesign and Analysis*, ed. B. Attaf, InTech, 2011.
21 C. Wang, X. Li and Y. Wang, Atlantis Press, 2017.
22 O. Madelung, in *Semiconductors: Data Handbook*, Springer Berlin Heidelberg, Berlin, Heidelberg, 2004, p. 691.
23 T. Tinoco, A. Polian, D. Gómez and J. P. Itié, *phys. stat. sol. (b)*, 1996, **198**, 433–438.
24 H. Ma, J. Zhang, B. Zhao, Q. Wei and Y. Yang, *AIP Advances*, 2017, **7**, 065007.
25 J. Li, Y. Qi, M. Zhang, Y. Zhou and X. Li, *Surface Science*, 2014, **624**, 1–7.
26 R. Liu, X. Yin, K. Feng and R. Xu, *Computational Materials Science*, 2018, **149**, 373–378.
27 J. C. Boettger, *Phys. Rev. B*, 1994, **49**, 16798–16800.
28 Y. Foulon and C. Priester, *Physical Review B*, 1992, **45**, 6259–6262.
29 R. L. Hayes, M. Ortiz and E. A. Carter, *Phys. Rev. B*, 2004, **69**, 172104.
30 S. P. Kowalczyk, J. T. Cheung, E. A. Kraut and R. W. Grant, *Phys. Rev. Lett.*, 1986, **56**, 1605–1608.
31 V. Kumar and B. S. R. Sastry, *Cryst. Res. Technol.*, 2001, **36**, 565–569.
32 A. S. Verma, *Philosophical Magazine*, 2009, **89**, 183–193.
33 M. Courel, J. A. Andrade-Arvizu and O. Vigil-Galán, *Appl. Phys. Lett.*, 2014, **105**, 233501.
34 H. Sun, Y. J. Park, K.-H. Li, X. Liu, T. Detchprohm, X. Zhang, R. D. Dupuis and X. Li, *Applied Surface Science*, 2018, **458**, 949–953.
35 M. Morkel, L. Weinhardt, B. Lohmüller, C. Heske, E. Umbach, W. Riedl, S. Zweigart and F. Karg, *Appl. Phys. Lett.*, 2001, **79**, 4482–4484.
36 C. Platzer-Björkman, J. Lu, J. Kessler and L. Stolt, *Thin Solid Films*, 2003, **431–432**, 321–325.
37 C. Cai, Y. Zhao, S. Xie, X. Zhao, Y. Zhang, Y. Xu, C. Liang, Z. Niu, Y. Shi, Y. Li and R. Che, *Small*, 2019, **15**, 1900837.
38 R. F. W. Bader and H. Essén, *The Journal of Chemical Physics*, 1984, **80**, 1943–1960.
39 E. Espinosa, I. Alkorta, J. Elguero and E. Molins, *The Journal of Chemical Physics*, 2002, **117**, 5529–5542.
40 S.-H. Wei and A. Zunger, *Applied Physics Letters*, 1998, **72**, 2011–2013.
41 S. Wei and A. Zunger, *Applied Physics Letters*, 1993, **63**, 2549–2551.
42 A. Crovetto and O. Hansen, *Solar Energy Materials and Solar Cells*, 2017, **169**, 177–194.
43 L. Yu, R. S. Kokenyesi, D. A. Keszler and A. Zunger, *Adv. Energy Mater.*, 2013, **3**, 43–48.
44 L. Yu and A. Zunger, *Phys. Rev. Lett.*, 2012, **108**, 068701.